nature research

https://doi.org/10.1038/s41929-020-00550-5

Supplementary information

Oxygen evolution reaction over catalytic single-site Co in a well-defined brookite TiO_2 nanorod surface

In the format provided by the authors and unedited

Supplementary Information

Oxygen Evolution Reaction over Catalytic Single-Site Co in a Well-Defined Brookite TiO_2 Nanorod Surface

Chang Liu[1, #], Jin Qian[2, #], Yifan Ye[3], Hua Zhou[4], Cheng-Jun Sun[4], Colton Sheehan[1], Zhiyong Zhang[1], Gang Wan[5], Yi-Sheng Liu[3], Jinghua Guo[3], Shuang Li[6], Hyeyoung Shin[2], Sooyeon Hwang[6], T. Brent Gunnoe[1], William A. Goddard III[2, *], Sen Zhang[1, *]

[1] Department of Chemistry, University of Virginia, Charlottesville, Virginia 22904, USA;

[2] Materials and Process Simulation Center, California Institute of Technology, Pasadena, California 91125, USA;

[3] Advanced Light Source, Lawrence Berkeley National Laboratory, Berkeley, California 94720, USA;

[4] X-ray Science Division, Advanced Photon Source, Argonne National Laboratory, Lemont, Illinois 60439, USA;

[5] Materials Science Division, Argonne National Laboratory, Lemont, Illinois 60439, USA;

[6] Center for Functional Nanomaterials, Brookhaven National Laboratory, Upton, New York 11973, USA

[#] These authors contributed equally.

* Corresponding Authors:

Email for W.A.G.: wag@wag.caltech.edu

Email for S.Z.: sz3t@virginia.edu

Supplementary Methods

Synthesis of cobalt-oleate and other metal-oleate complex. The cobalt–oleate complex was obtained by reacting cobalt chloride ($CoCl_2 \cdot 6H_2O$) and sodium oleate. 4.75 g of $CoCl_2 \cdot 6H_2O$ (20 mmol, Acros Organics, 98%) and 12.2 g of sodium oleate (40 mmol, TCI, 95%) were dissolved in a mixture solvent of ethanol (40 mL), deionized water (30 mL) and hexanes (70 mL). The solution was heated to 60 °C and maintained at the temperature for 4 hours. The upper purple liquid layer with the cobalt–oleate complex was then washed three times with deionized water (30 mL) in a separatory funnel. The hexanes in cobalt-oleate dispersion was removed by rotate-evaporation. The obtained cobalt-oleate complex was in a waxy form, which was dissolved in a mixture of pre-dried ODE and OAc (1.0 M) with a concentration of 0.2 M. Other metal-oleate complexes were prepared using the similar route of Co-oleate complex, as reported in our previous work.[1]

Synthesis of carbon supported CoO nanoparticles. Co nanoparticles were first obtained via the thermal decomposition of $Co_2(CO)_8$, according to the reported method.[2] Briefly, 18 mL of tetralin was first mixed with 0.35 mL of OAc and 0.5 mL of dioctylamine, and purged with N_2 at 110 ºC for 0.5 h. After the solvent was cooled to room temperature, 0.54 g of $Co_2(CO)_8$ was swiftly added into the above mixture. The system was maintained at 100 ºC for 20 min, then quickly heated up to 210 ºC at 15 °C min^{-1}, and kept at this temperature for 30 min. The Co nanoparticles were collected by centrifugation at 8000 rpm for 8 min with addition of excessive ethanol, and were further purified twice by the addition of hexane and ethanol. The as-prepared Co nanoparticles was then loaded on Vulcan-72 carbon by sonicating nanoparticles with appropriate amount of Vulcan-72 carbon in hexanes, followed by centrifugation at 8000 rpm for 8 min. The carbon supported Co was dried under vacuum for overnight and annealed in air at 200 °C overnight to obtain the carbon supported CoO nanoparticles.

Vertical alignment of Co-TiO_2 nanorods. The vertical alignment of Co-TiO_2 nanorods was obtained through the self-assembly process, similar to our previous report .[1] Briefly, the as-synthesized Co-TiO_2 nanorods were dispersed in hexane with a concentration of 60 mg mL^{-1}. The hexane dispersion of Co-TiO_2 nanorods (10 μL) was drop-cast on the surface of diethylene glycol (DEG) in a Teflon well. The Teflon well was covered with a glass slide for slow evaporation of hexane. With a 2 hours evaporation of hexane, one monolayer of vertically aligned Co-TiO_2 nanorods was formed on the surface of DEG, which could be transferred on TEM grid. The TEM grid was dried to remove DEG in vacuum at the room temperature.

Example of GCQM calculation. VASP is fast for plane wave DFT, but its solvation method is not so accurate. jDFTx has an excellent validated solvation model (CANDLE), which has been properly benchmarked to experiment, such as agreement through radial distribution functions, solvation energies, and potential of zero charge (PZC) of numerous electrochemical systems.[3] However, jDFTx is much slower and less convenient. Thus, we use VASP to carry out constant electron calculations with VASPsol. Subsequently. we use jDFTx to obtain the more accurate constant potential using the CANDLE solvation. Then we use the Legendre transformation developed in our recent study to convert from constant electron to constant potential.[4] A specific example is summarized in **Supplementary Table 2**, state 1-9 are referring to the different intermediate states along the energetically most favorable adsorbate evolution mechanism (AEM) pathway shown in **Fig. 5** of the manuscript. Our computational steps progress from the left column (dE(VASP)) to the right column (dG). We first performed geometry optimization in VASP with VASPsol, leveraging the speed and parallelization advantage of VASP, and obtained the values in dE(VASP) column. It is worth noting is that these numbers dE(VASP) by themselves are not meaningful for electrochemical systems because they are calculated at neutral condition. We then

used the optimized structures obtained in VASP as the starting point for single point energy calculation in jDFTx, leveraging the jDFTx's specially developed CANDEL solvation model and constant potential method best suited for electrochemistry applications. Next, we used the GCP-K method developed in reference,[4] which is a Legendre transform relating the net charge of the system to the applied voltage, and the results under the target potential 1.63 V vs. RHE are shown in dE(jDFTx) column. GCP-K allows us to connect to the traditional Butler–Volmer kinetics, and with the last step of including the entropic correction -dTS term, we can directly compare dG (which equals dE(jDFTx) - dTS) with experiment, under the experimental solvation and potential condition. In **Supplementary Table 2**, we provided results under pH = 14, 1.63 V vs. RHE as an example. Similarly, we can carry out the calculation under any pH or potential condition using GCP-K method. The dG numbers are what we used in plotting **Fig. 5**.

GCQM calculation comparison of different Co single-site configuration. As shown in **Supplementary Fig. 24**, we found that placing the surface Co at the 5C Ti site, rather than 6C Ti, is more stable by 0.25 eV. In order to determine where to place the 2nd and 3rd layer Co, we examined both the case of the 2nd and 3rd layer Co's connecting directly to the 1st layer via O and the non-connecting case. We found that connecting the Co dopants by O in a line is 0.15eV more stable than having them separated. Despite the fact that Co in a line configuration is calculated to be more stable, we further carried out three groups of OER GCQM kinetics comparison studies to assess different Co configurations.

Group 1. Co single site on the top layer of the catalyst (**Supplementary Fig. 24a**)

Group 2. Three Co single site connecting in a line configuration (**Supplementary Fig. 24c**)

Group 3. Three Co single site not in a line configuration (**Supplementary Fig. 24d**)

The GCQM calculation results based on Group 1 and 3 are summarized in **Supplementary Tables 3** and **4**, while the result for Group 2 is present in **Supplementary Table 2**. For each model, all energetics are referenced to the initial state 1. The atomic illustrations for the adsorbates in state 1-9 are same as those in **Fig. 5** in the manuscript. We use the values from the dG columns for free energy landscape at a potential 1.63 V vs. RHE. The density of states (DOS) analysis has been supplied here for group 1-3 and is plotted against E-Efermi (with Efermi at 0 V) (**Supplementary Fig. 29-31**). The d-band broadening and a lower d-band center for Ti has been observed in group 2 and 3. Group 2 shows a high Co d orbital DOS at Efermi, indicating that the Co active site in group 2 has a higher probability of d electron transfer and bonding. Group 3 Co d orbital DOS is also higher than group 1. All 3 groups have a much higher Co d orbital DOS than Ti d orbital DOS at Efermi, confirming that Co is more likely to be the active site than Ti in this reaction.

Using GCQM calculations, we found that the rate determining step (RDS) is consistent over all 3 groups (state 3 TS) in the interested potential range. Correspondingly, the Tafel Slope for all 3 groups is 74 mV dec^{-1}, in agreement with experimental result (72 mV dec^{-1}). Second, the energetics for the RDS are 0.63, 0.61 and 0.57 eV over 3 groups, respectively. They are fluctuating within the accuracy of 0.05 eV of GCQM calculations, which is already the best level of accuracy can be achieved computationally with full kinetics. Based on energetics, the expected TOFs are 151.3 s^{-1} over group 1, 307.4 s^{-1} over group 2, and 1547.9 s^{-1} over group 3 at 1.63 V vs. RHE. The variation is also within the accuracy of GCQM calculations. The TOF for group 2 (the most stable structure) of 307.4 s^{-1} is in excellent agreement with the experimental value. Group 2 is expected to be the dominate structure in concentration at the target oxidation potential (1.53 – 1.63 V vs. RHE) after stabilization and hence was the most relevant case considered in the manuscript.

GCQM calculation for specific capacitance of Co-TiO_2. our GCQM formulism enables the direct calculation of specific capacitance at operando conditions while including solvation.[4] The grand canonical potential $GCP(U)$ for the electrochemical process has the form:

$$GCP(U) = F(n) - ne(U_{SHE} - U) \quad (1)$$

where we can convert SHE to the experimental RHE reference, where F is the Helmholtz Energy, n is the number of electrons that are being optimized, and U is the applied potential.

Further simplification leads to the quadratic form,

$$GCP(U) = \frac{-1}{4a}(b - \mu + eU)^2 + c - n_0\mu + n_0eU \quad (2)$$

which allows us to correlate parameters a, b, c to the physical macroscopically observable properties, including the capacitance C_s,

$$GCP(U) = \frac{e^2C_s}{2}(U - U_{pzc})^2 + n_0eU + F_0 - n_0\mu \quad (3)$$

This leads to C_s= 18.2 μF cm^{-2} under *operando* conditions for Co-TiO_2 with the (210) surface and 12.5% Co doping content. This is very close to the value for TiO_2 materials (25 μF cm^{-2}).[5] We have used this specific capacitance to calculate ECSAs, current densities and TOFs.

Supplementary Tables 1-4

Supplementary Table 1. Structural parameters of TiO_2 and Co-TiO_2 nanorods obtained from Ti K-edge and Co K-edge EXAFS spectra. The uncertainty in CN fitting parameter is defined as the amount by which the parameter can be flexibly changed, meanwhile allowing the flexibility of the other fitting parameters, without dramatically worsening the fit.

	Sample	Path	R (Å)	CN	ΔR (Å)	σ^2 (10^{-3} Å)	R-factor
Ti K-edge	TiO_2	Ti-O	1.936	3.4 ± 0.3	0.056	0.0061	0.0176
		Ti-Ti	3.048	7.5 ± 0.6	0.058	0.00456	0.0161
	Co-TiO_2	Ti-O	1.963	3.4 ± 0.3	0.0833	0.01383	0.00367
		Ti-Ti/Co	3.054	7.7 ± 0.6	0.0633	0.01407	0.00458
Co K-edge	Co-TiO_2 (0.92 V)	Co-O	1.998	3.4 ± 0.3	0.1337	0.00266	0.00705
		Co-Ti/Co	3.132	6.6 ± 0.6	0.0674	0.0211	0.012
	Co-TiO_2 (1.12 V)	Co-O	2.007	3.7 ± 0.2	0.142	0.00901	0.00126
		Co-Ti/Co	3.126	7.5 ± 0.5	0.0619	0.03769	0.00453
	Co-TiO_2 (1.27 V)	Co-O	2.003	3.7 ± 0.2	0.138	0.00677	0.00946
		Co-Ti/Co	3.134	7.1 ± 0.5	0.0704	0.0269	0.00519
	Co-TiO_2 (1.43 V)	Co-O	2.006	3.9 ± 0.2	0.141	0.00999	0.00347
		Co-Ti/Co	3.124	7.1 ± 0.4	0.0604	0.03877	0.0178
	Co-TiO_2 (1.57 V)	Co-O	2.003	4.3 ± 0.2	0.138	0.011	0.00437
		Co-Ti/Co	3.133	7.0 ± 0.4	0.0692	0.00545	0.01645

Supplementary Table 2. Energetics in eV along the most favorable pathway (AEM adsorption evolution mechanism) at target potential 1.63 V vs. RHE to illustrate the GCP-K method.

	dE(VASP)	dE(jDFTx)	-dTS	dG
State 1	0.00	0.00	0.00	0.00
State 2	5.57	0.48	-0.40	0.08
State 3 (TS)	6.31	1.05	-0.44	0.61
State 4	5.55	0.54	-0.26	0.29
State 5	10.10	0.03	-0.60	-0.56
State 6	15.14	0.03	-0.90	-0.87
State 7	25.27	-0.02	-0.99	-1.01
State 8	30.50	0.22	-1.35	-1.13
State 9	15.51	-0.48	-0.67	-1.15

Supplementary Table 3. Energetics in eV along the most favorable pathway for group 1: Co single site on the top layer of the catalyst.

	dE(VASP)	dE(jDFTx)	-dTS	dG
State 1	0.00	0.00	0.00	0.00
State 2	5.58	0.58	-0.35	0.23
State 3 (TS)	6.33	1.07	-0.44	0.63
State 4	5.67	0.65	-0.22	0.43
State 5	10.05	0.18	-0.56	-0.39
State 6	15.13	0.09	-0.91	-0.82
State 7	25.62	0.21	-0.97	-0.76
State 8	30.75	0.42	-1.31	-0.89
State 9	15.48	-0.47	-0.66	-1.13

Supplementary Table 4. Energetics in eV along the most favorable pathway for group 3: Co single sites not in a line configuration.

	dE(VASP)	dE(jDFTx)	-dTS	dG
State 1	0.00	0.00	0.00	0.00
State 2	5.56	0.46	-0.38	0.09
State 3 (TS)	6.23	1.02	-0.45	0.57
State 4	5.46	0.50	-0.28	0.22
State 5	9.95	0.00	-0.61	-0.61
State 6	15.14	0.08	-0.93	-0.84
State 7	25.52	0.18	-1.00	-0.82
State 8	30.56	0.44	-1.31	-0.87
State 9	15.47	-0.47	-0.68	-1.15

Supplementary Figures 1-31

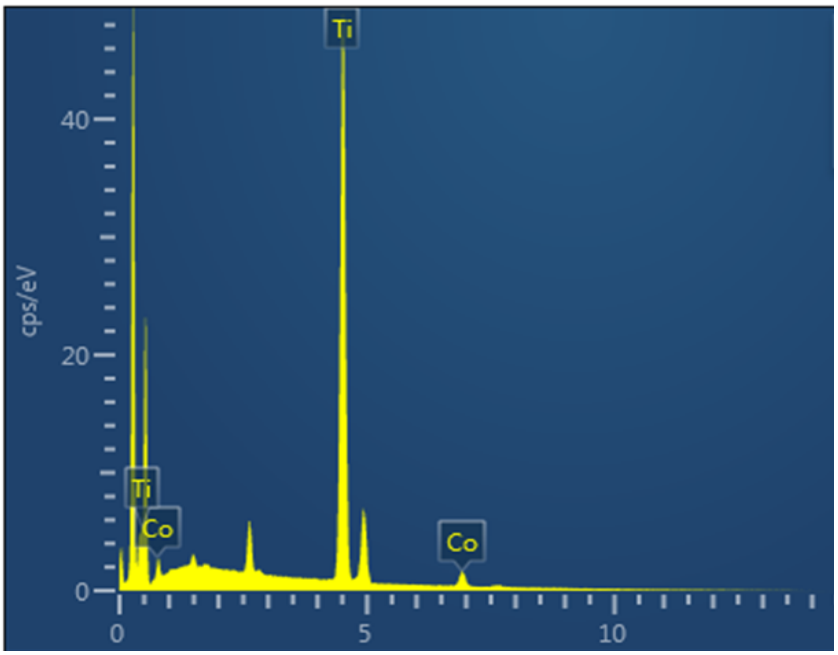

Supplementary Figure 1. EDS spectrum of Co-TiO_2 nanorods (12% Co).

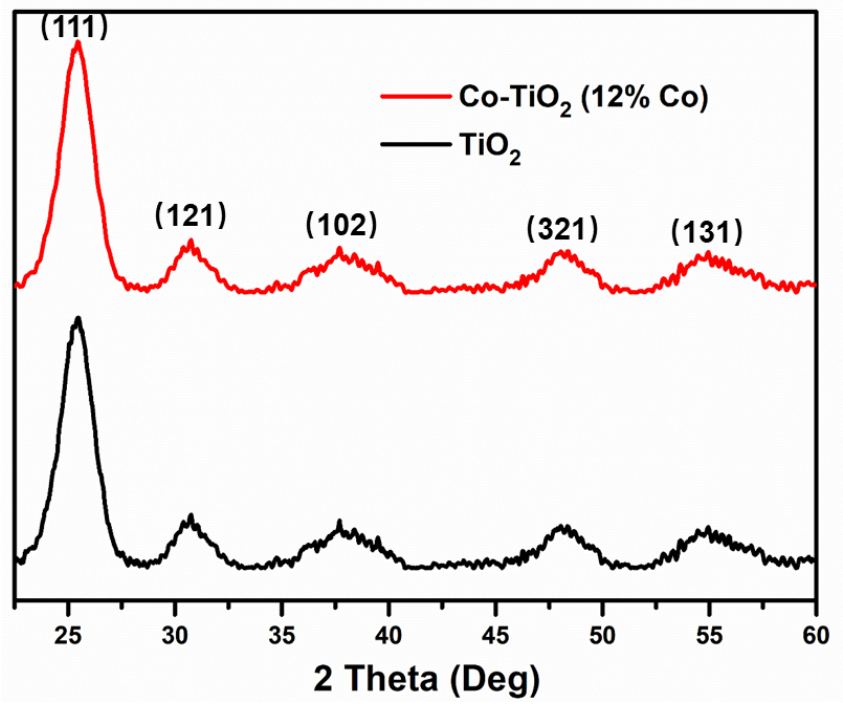

Supplementary Figure 2. XRD diffraction patterns of Co-TiO_2 nanorods (12% Co) and undoped TiO_2.

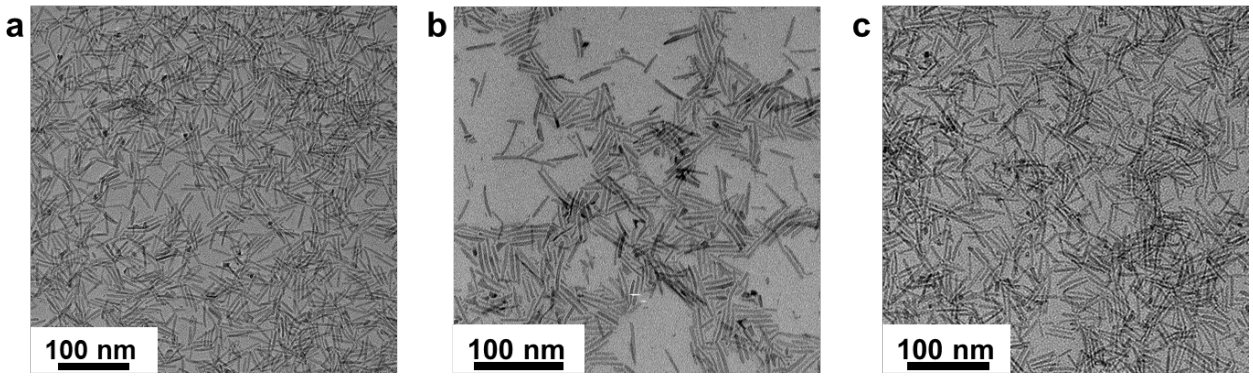

Supplementary Figure 3. TEM images of TiO_2 and Co-TiO_2 nanorods with different doping level. **a**, TiO_2; **b**, Co-TiO_2 (Co 4.2%); **c** Co-TiO_2 (Co 7.5 %).

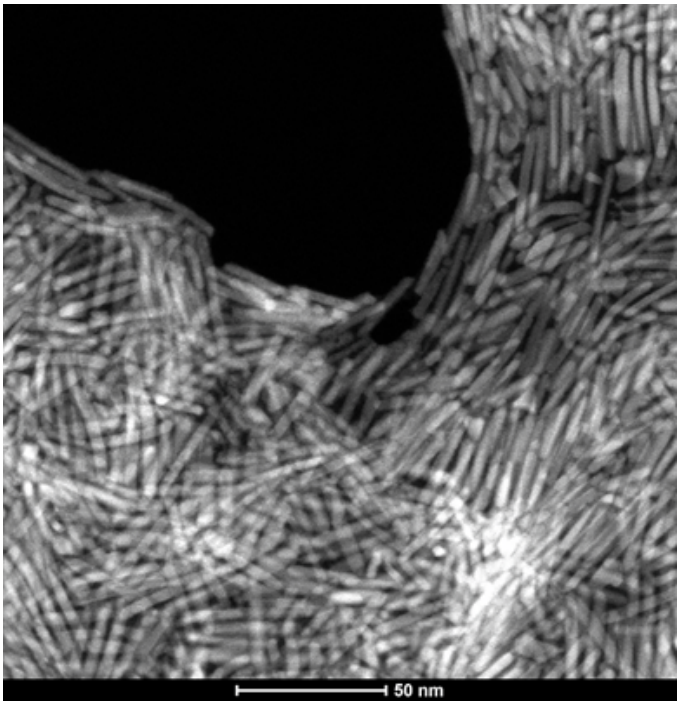

Supplementary Figure 4. HAADF STEM image of Co-TiO_2 nanorods (12% Co).

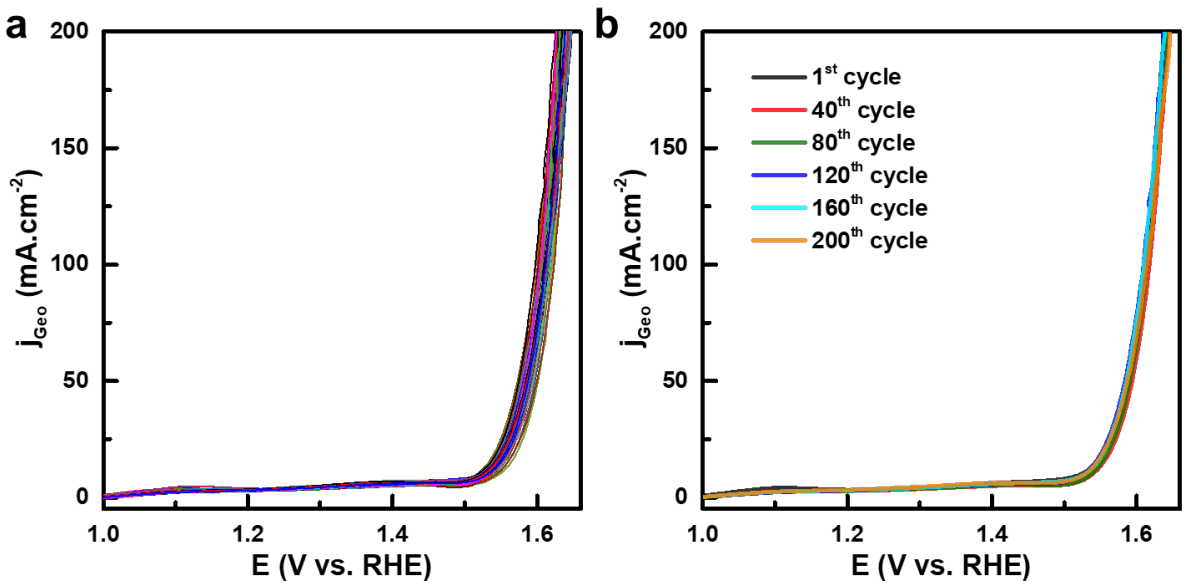

Supplementary Figure 5. Multiple LSV curves of Co-TiO_2 in 1.0 M KOH electrolyte at 10 mV s^{-1}. 200 continuous LSV curves were summarized in **a** with all of them overlapping and oscillating in a very narrow range. It is worth pointing out that the oscillation of repeated LSV in **a** is a natural fluctuation, due to the generation and release of oxygen bubbles from the electrodes that lead to small variations in local pH and mass transfer profile, rather than a sign of deactivation or monotonic activity loss. To further eliminate the visually misleading information from the oscillation, we highlighted the polarization curves of the 1st, 40th, 80th, 120th, 160th, 200th cycles in **b**. Clearly, these curves collected at fixed intervals are highly consistent with each other.

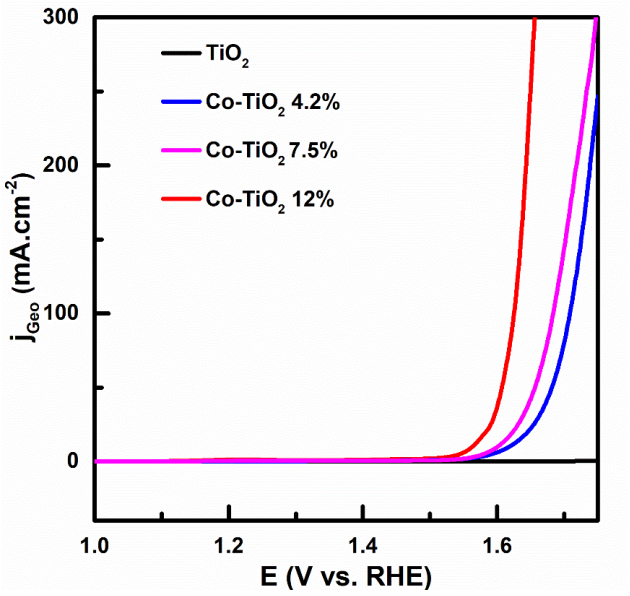

Supplementary Figure 6. LSV plots of Co-TiO_2 nanorods with different Co doping levels for the OER.

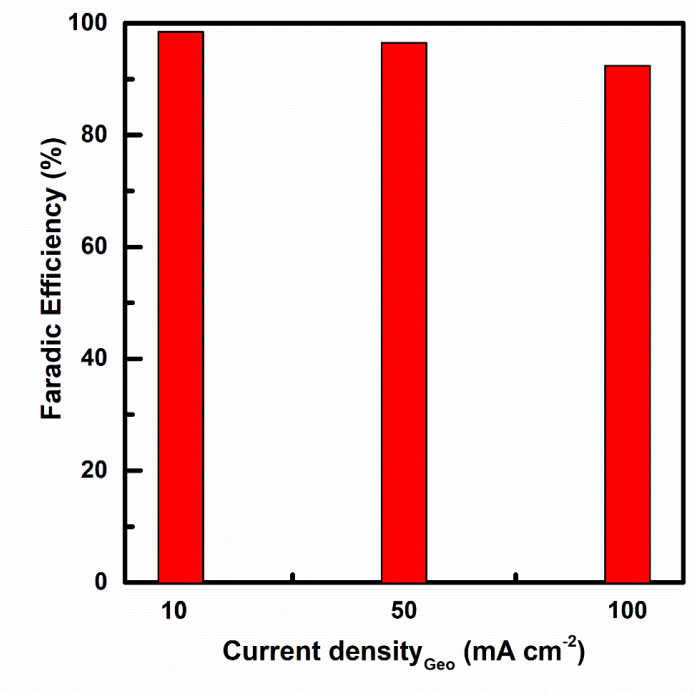

Supplementary Figure 7. Faradic efficiency of Co-TiO_2 nanorods at different geometric current densities.

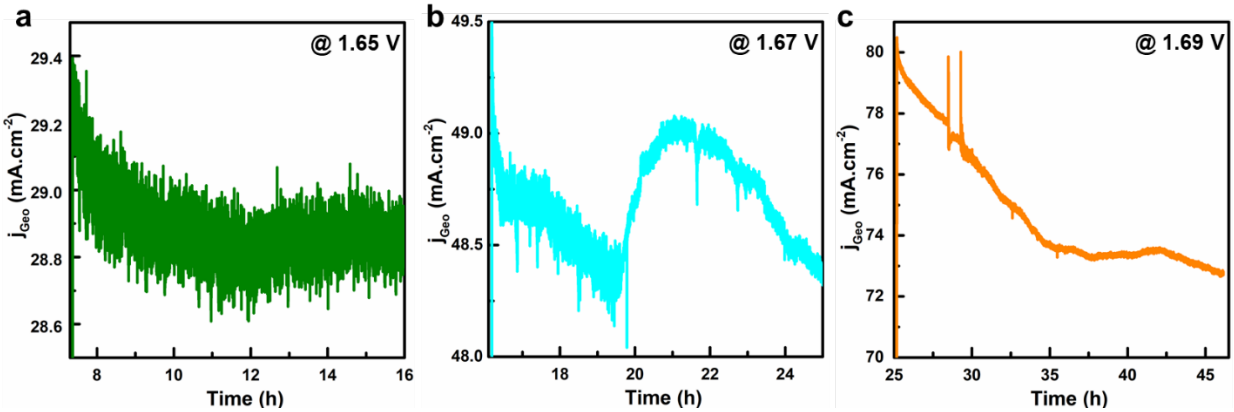

Supplementary Figure 8. The zoom-in view of CA results in Fig. 2c at 1.65 V (**a**), 1.67 V (**b**), and 1.69 V (**c**). All potentials in the CA measurement are applied without iR correction. The color code of CA curve matches with the related segment in Fig. 2c.

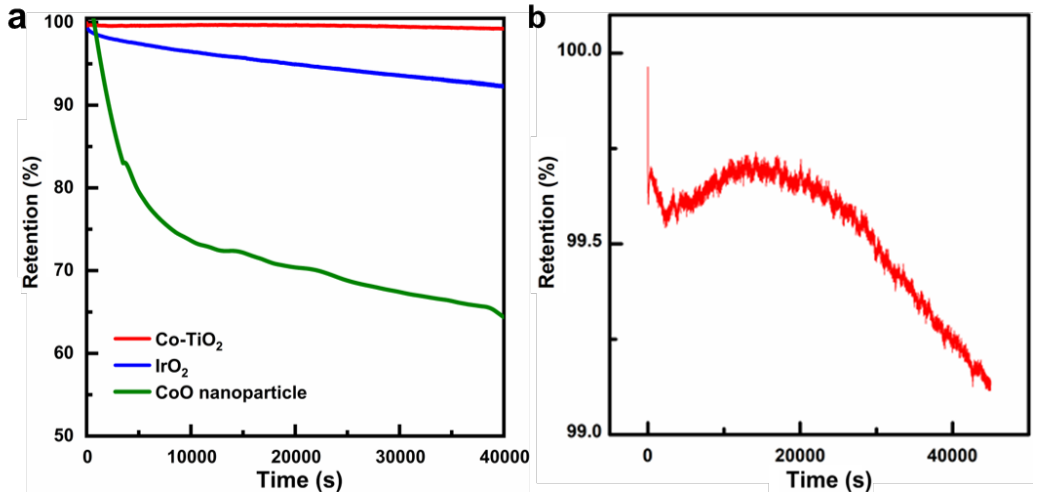

Supplementary Figure 9. a, The CA retention comparison of Co-TiO_2 nanorods, CoO and IrO_2 nanoparticles catalysts at 1.62 V vs. RHE. **b**, The zoom-in view of CA result of Co-TiO_2 catalyst.

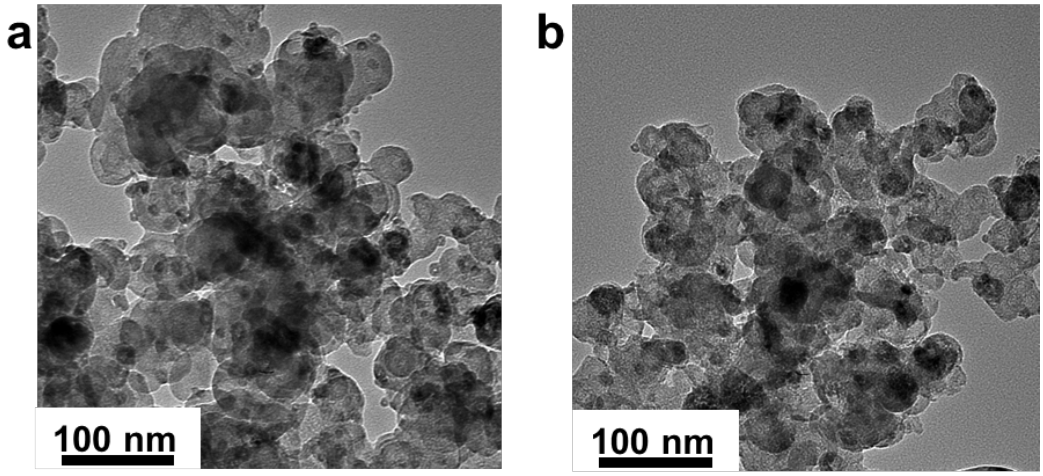

Supplementary Figure 10. TEM images of CoO nanoparticles on carbon **a** before and **b** after electrochemical test.

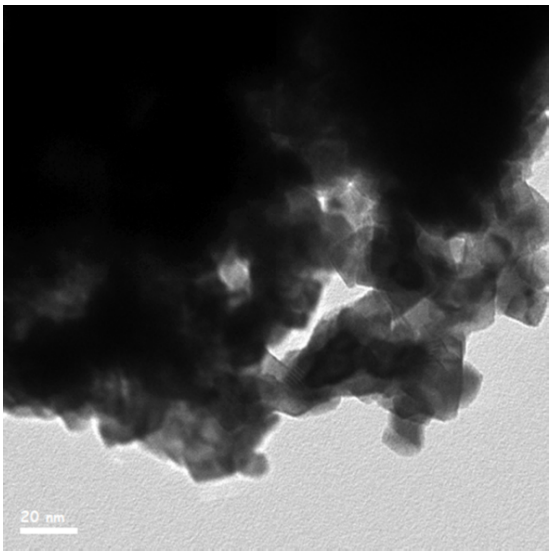

Supplementary Figure 11. TEM image of commercial IrO_2 nanoparticles on Carbon.

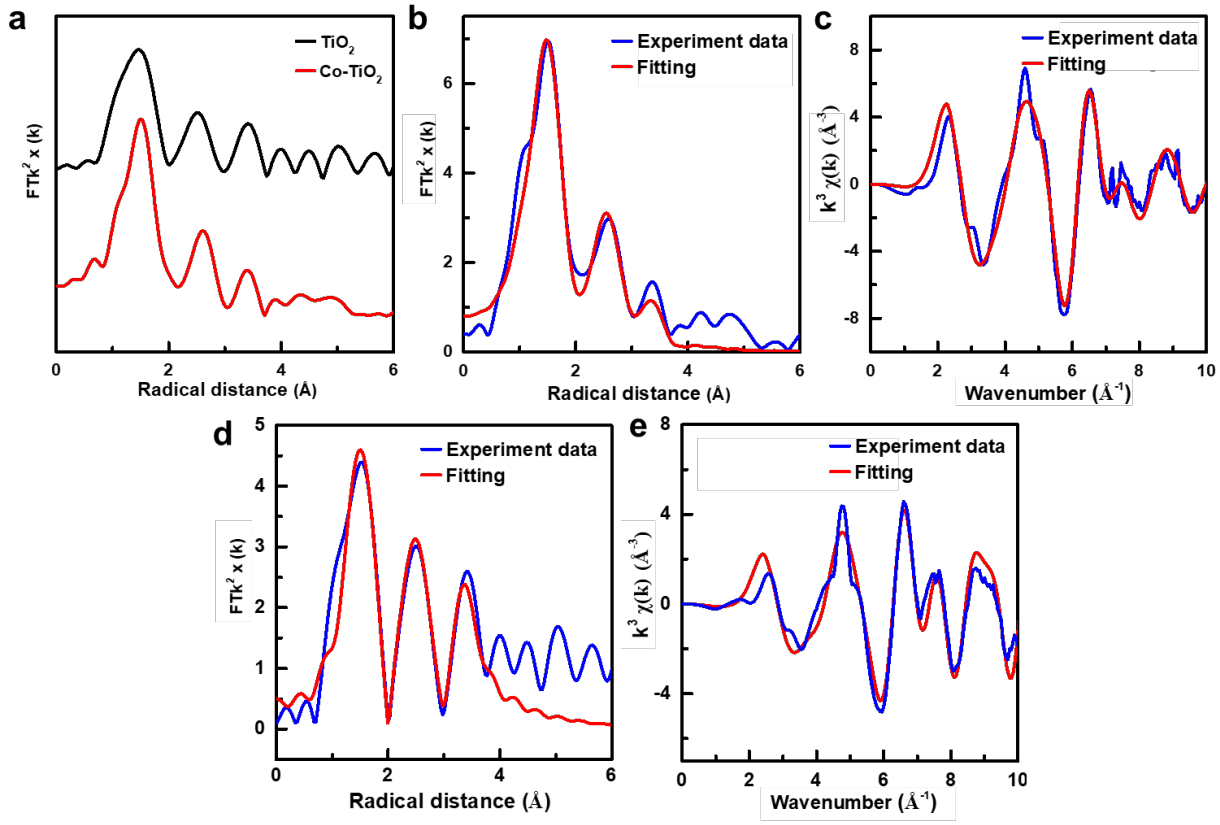

Supplementary Figure 12. Ti K-edge EXAFS spectra of TiO_2 and Co-TiO_2. **a,** Ti K-edge EXAFS spectra of TiO_2 and Co-TiO_2; **b,** Co-TiO_2 Ti K-edge EXAFS spectrum fitting in R-space; **c,** Co-TiO_2 Ti K-edge EXAFS spectrum fitting in k-space; **d,** TiO_2 Ti K-edge EXAFS spectrum fitting in R-space; **e,** TiO_2 K-edge EXAFS spectrum fitting in k-space.

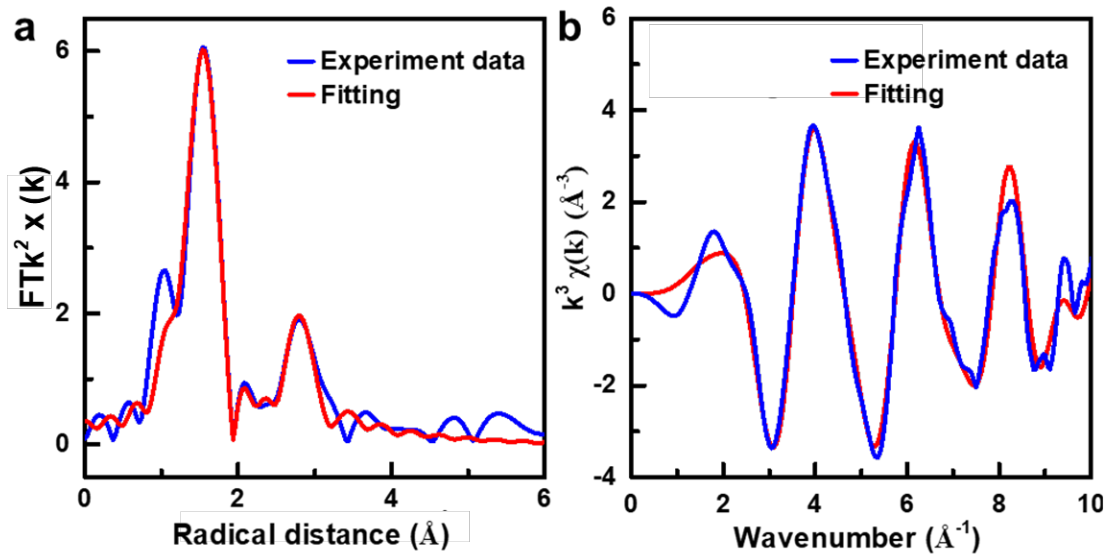

Supplementary Figure 13. Co K-edge EXAFS spectra fittings for Co-TiO_2 at 0.92 V vs. RHE. **a,** Fitting in R-space; **b,** Fitting in k-space.

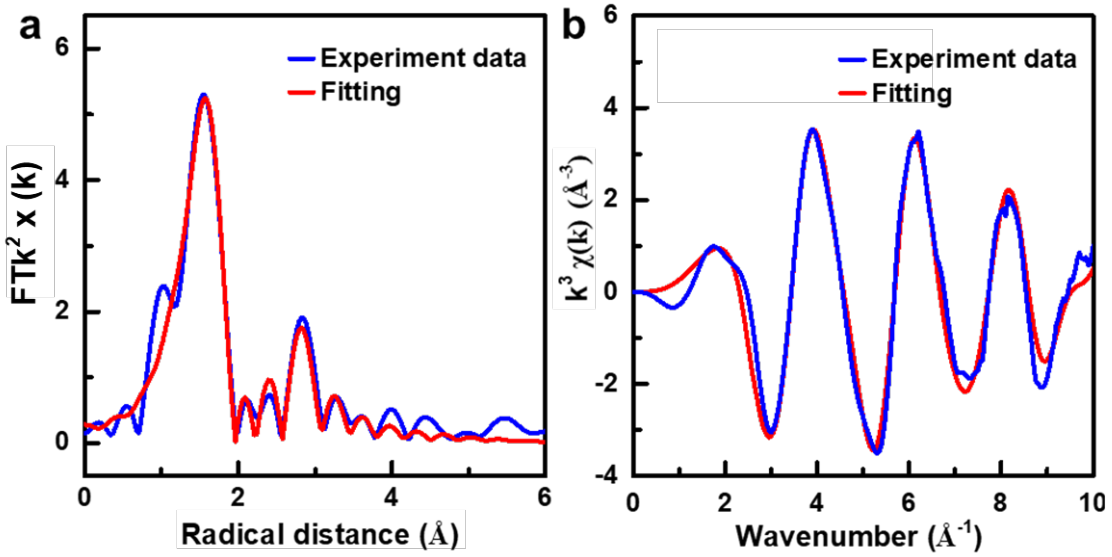

Supplementary Figure 14. Co K-edge EXAFS spectra fittings for Co-TiO_2 at 1.12 V vs. RHE. **a,** Fitting in R-space; **b,** Fitting in k-space.

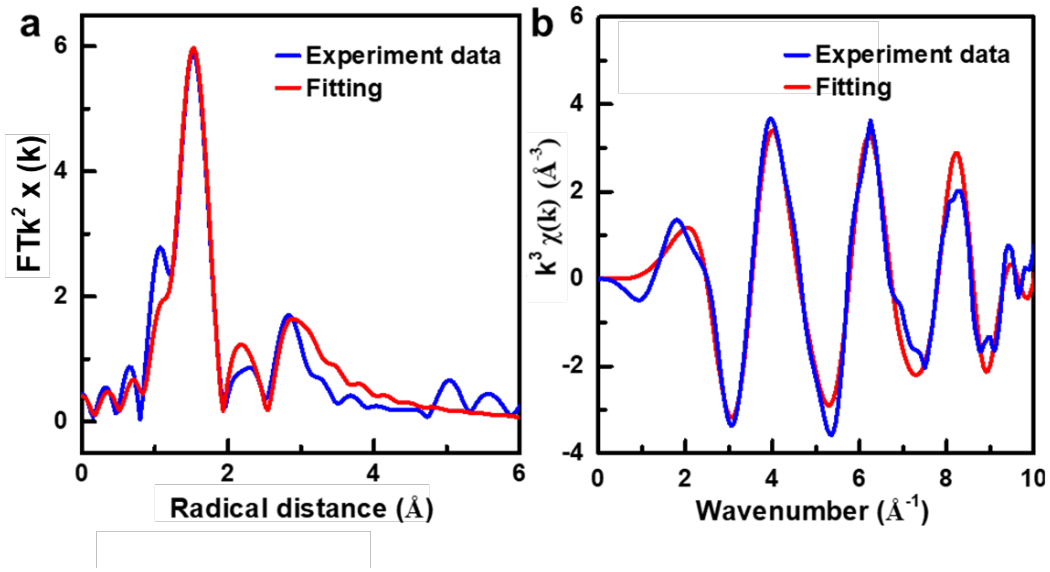

Supplementary Figure 15. Co K-edge EXAFS spectra fittings for Co-TiO_2 at 1.27 V vs. RHE. **a,** Fitting in R-space; **b,** Fitting in k-space.

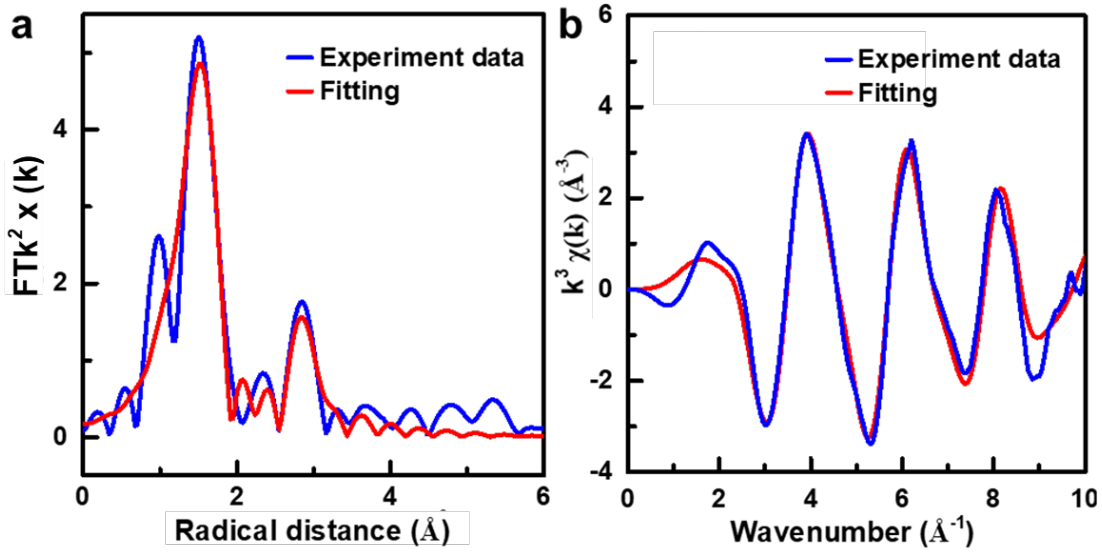

Supplementary Figure 16. Co K-edge EXAFS spectra fittings for Co-TiO_2 at 1.43 V vs. RHE. **a,** Fitting in R-space; **b,** Fitting in k-space.

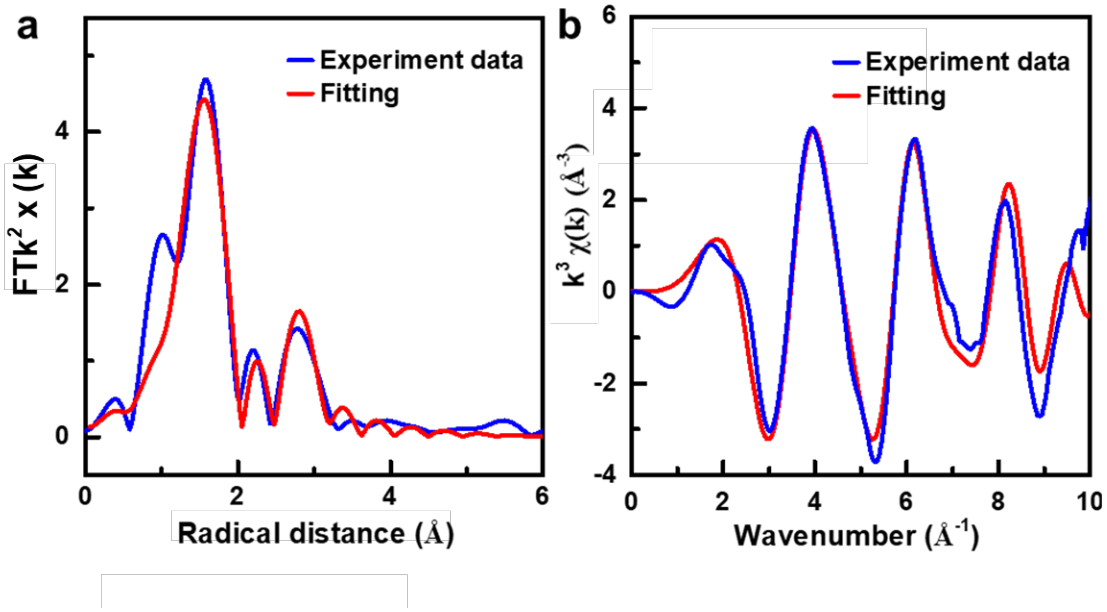

Supplementary Figure 17. Co K-edge EXAFS spectra fittings for Co-TiO_2 at 1.57 V vs. RHE. **a,** Fitting in R-space; **b,** Fitting in k-space.

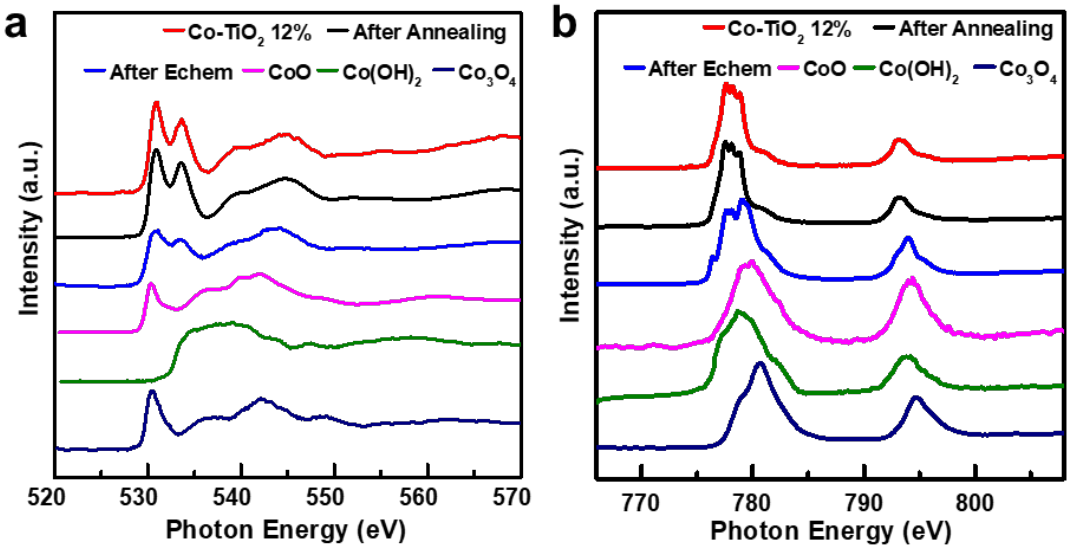

Supplementary Figure 18. XAS with soft-X-ray excitation for Co-TiO_2 and reference samples. **a**, O K-edge XAS; **b**, Co L-edge XAS.

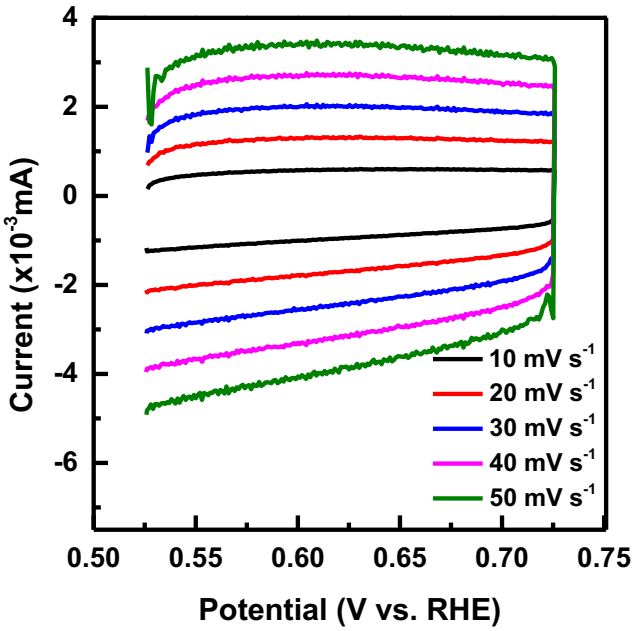

Supplementary Figure 19. Cyclic voltammetry plots of Co-TiO_2 catalyst at different scanning rates in the potential window of 0.526 V - 0.726 V vs. RHE.

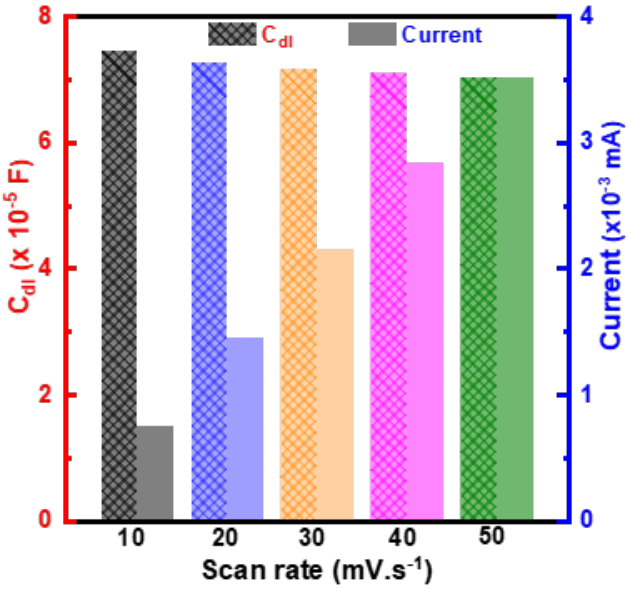

Supplementary Figure 20. Capacitive current and corresponding double-layer capacitance of Co-TiO_2 (12%) modified electrode at different scanning rates.

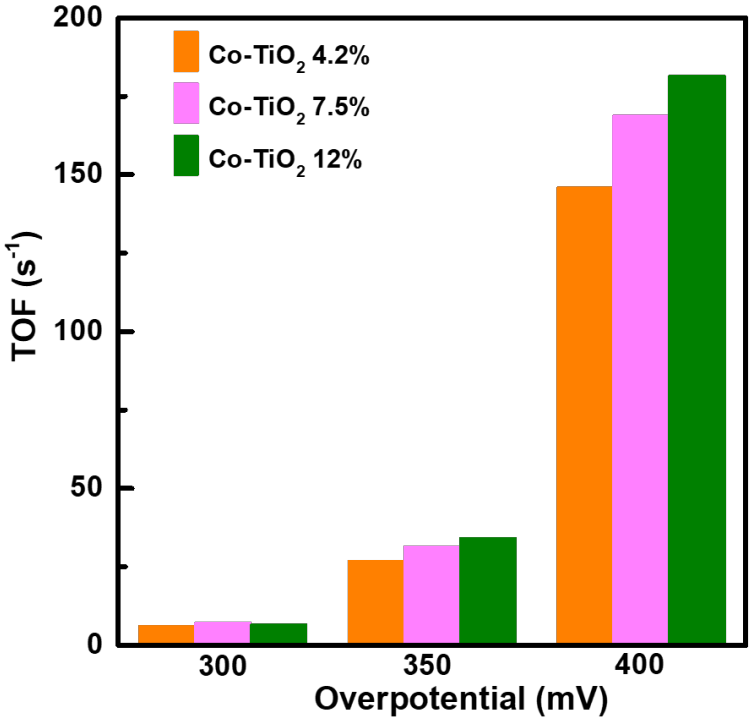

Supplementary Figure 21. TOFs of Co-TiO_2 nanorods with different Co content.

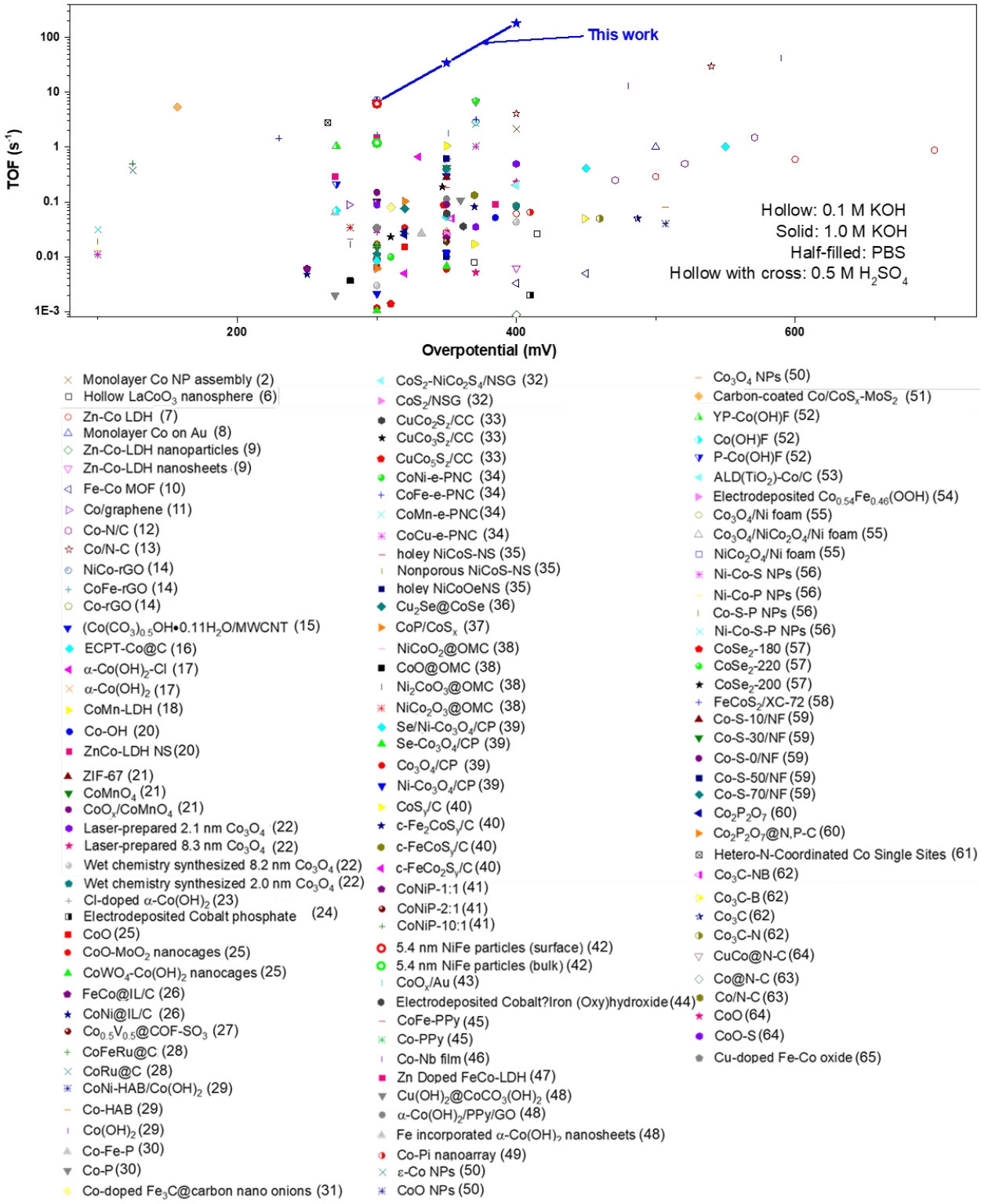

Supplementary Figure 22. Comparison of the TOF values in the present work with previous reported results of Co-based OER catalysts (All references are listed in Supplementary Reference)

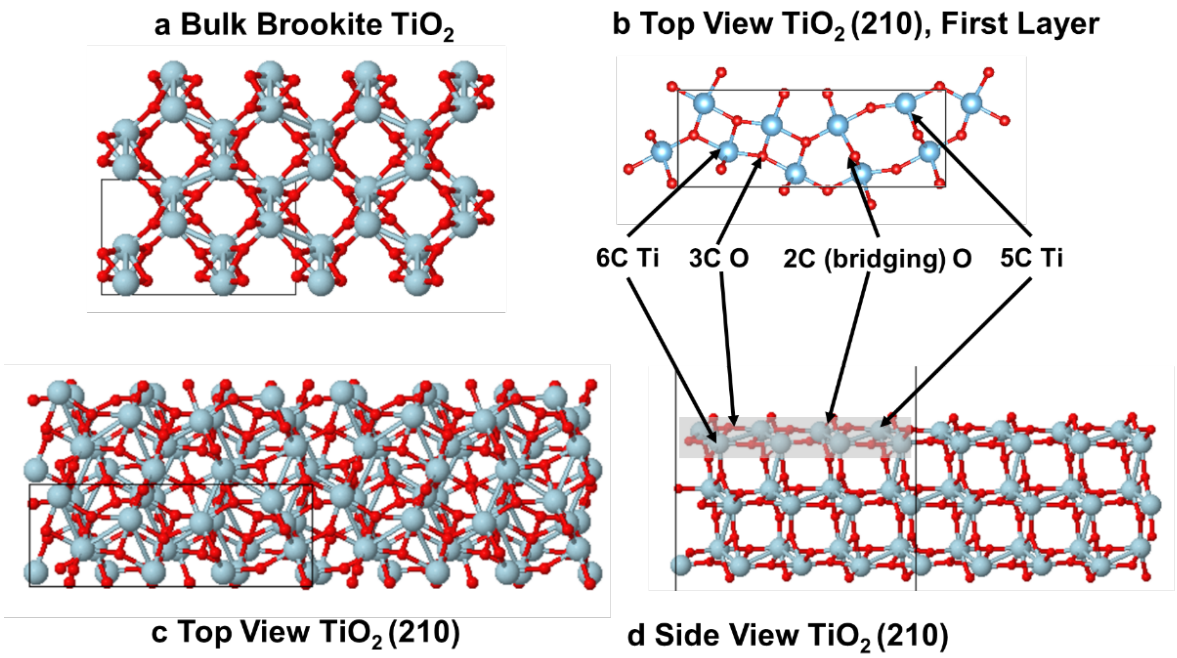

Supplementary Figure 23. Slab models of the brookite-phase TiO_2 structure. Blue and red circles denote Ti and O atoms respectively. **a**, bulk brookite TiO_2 structure with experimental lattice parameter at 298 K of a = 9.174 Å, b = 5.449 Å, c = 5.168 Å. **b**, top view of TiO_2 (210) surface, which corresponds to the grey shaded area in (d). There are two types of Ti on this surface: 6 coordinate Ti (denoted "6C") and 5 coordinate Ti (denoted "5C"). The 6C Ti is lower on z axis, as shown in (d), while 5C Ti is higher on z axis. Similarly, there are two types of O on this surface, 3 coordinate O (3C-O) as in the bulk sitting lower on the z axis, and bridging O (2C-O) sitting higher on the z axis. **c**, Top view of the TiO_2 (210) surface. **d**, Side view of the TiO_2 (210) surface, the vertical axis is z axis.

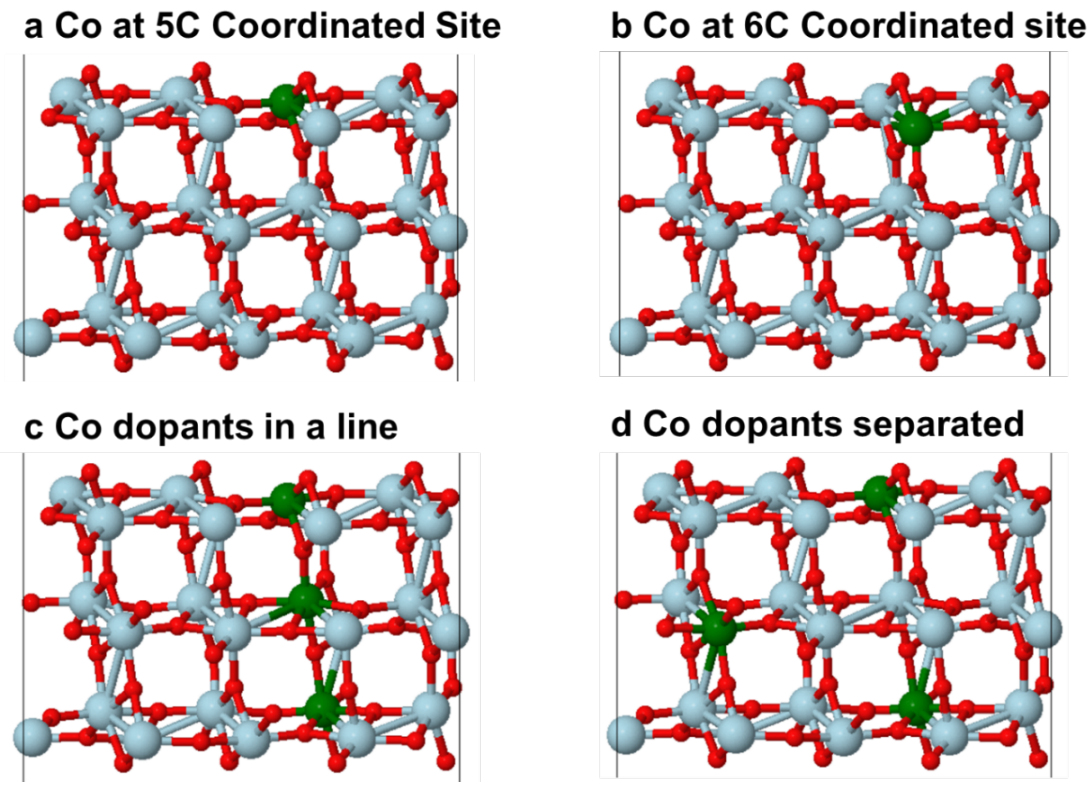

Supplementary Figure 24. Thermodynamic stability of Co dopant at various sites. Blue, red and green circles denote Ti, O and Co atoms, respectively. We find that Co on the first layer has the largest effect on the OER mechanism. **a**, Co dopant at 5C position is 0.25 eV more stable than (b). **b**, Co dopant at 6C position. After deciding that the 5C coordinated position is energetically favorable, we need to establish the position of Co dopants for second and third layer. **c**, Co dopants along a line is 0.15 eV more stable than (d). **d**, Co dopants in second layers not in a line. Thus, we chose Co dopants in a line with 5C position on the first layer (c) as the starting point for GCQM calculations in main text, while the comparison and discussion between c and d are included in supplementary method and tables.

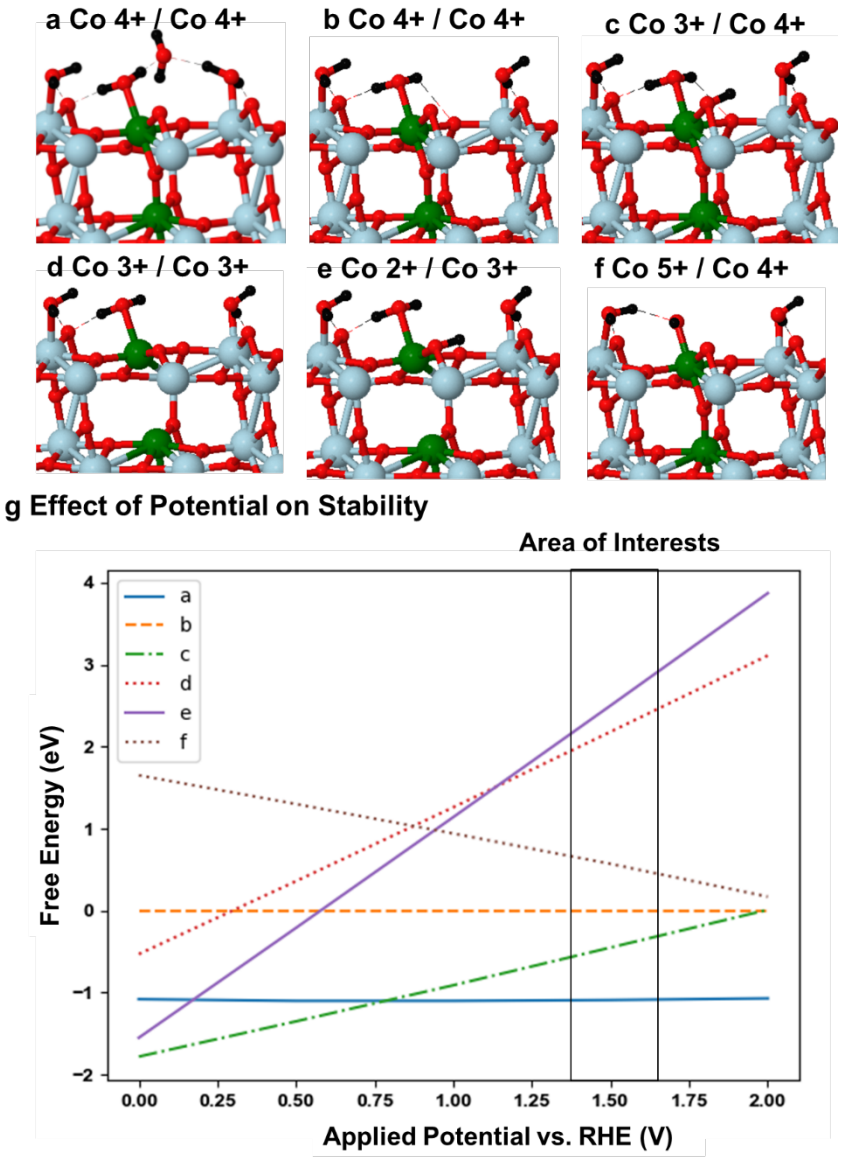

Supplementary Figure 25. a-f, Various structures with various Co oxidation states based on stoichiometry. Blue, red, green and black circles denote Ti, O, Co and H atoms, respectively. Starting from the H_2O covered structure, removing lattice oxygen or adding interstitial hydrogen creates Co with the lower oxidation state abundant in bulk TiO_2. We take the structure a as the reference state at 0 eV. The extra unpaired spin on the bridging oxygen in structure b (circled) provides possibility for O-O coupling, which motivated us to examine the LOM mechanism in addition to the AEM mechanism we found to dominate. The hydrogen interstitial is most sensitive to the change of pH, becomes less stable at higher pH. We fix the pH at strong basic conditions, to reflect the experimental working condition. **g**, Effect of applied potential on the stability of structures a-f at pH = 14. As the applied potential increases, lower oxidation state such as Co^{2+}, and Co^{3+} become less stable, so that structure a became the most stable one. The stability is obtained by comparing the free energy of different structures with structure a.

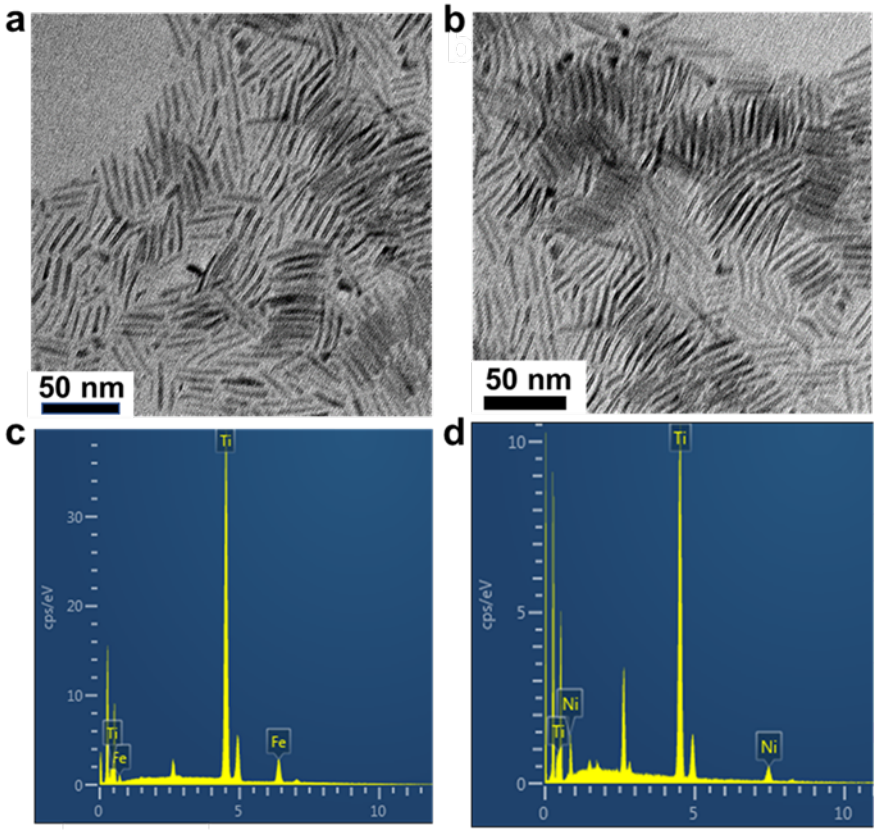

Supplementary Figure 26. Morphology and composition characterization of Fe-TiO_2 and Ni-TiO_2 nanorods. **a**, TEM image of Fe-TiO_2. **b**, TEM image of Ni-TiO_2. **c**, EDS spectrum of Fe-TiO_2 nanorods (Fe 12% doping). **d**, EDS spectrum of Ni-TiO_2 nanorods (Ni 11% doping).

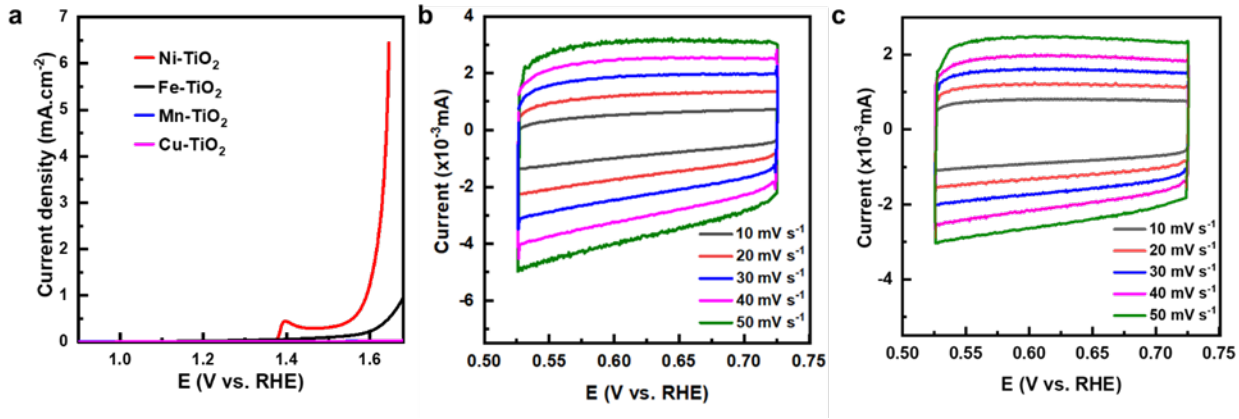

Supplementary Figure 27. a, LSV plots of Ni-TiO_2, Fe-TiO_2, Mn-TiO_2 and Cu-TiO_2 nanorods for the OER. **b**, CV plots of Fe-TiO_2 catalyst at different scanning rates in the potential window of 0.526 V - 0.726 V vs. RHE in N_2-saturated KOH electrolyte; **c**, CV plots of Ni-TiO_2 catalyst at

different scanning rates in the potential window of 0.526 V - 0.726 V vs. RHE in N_2-saturated KOH electrolyte.

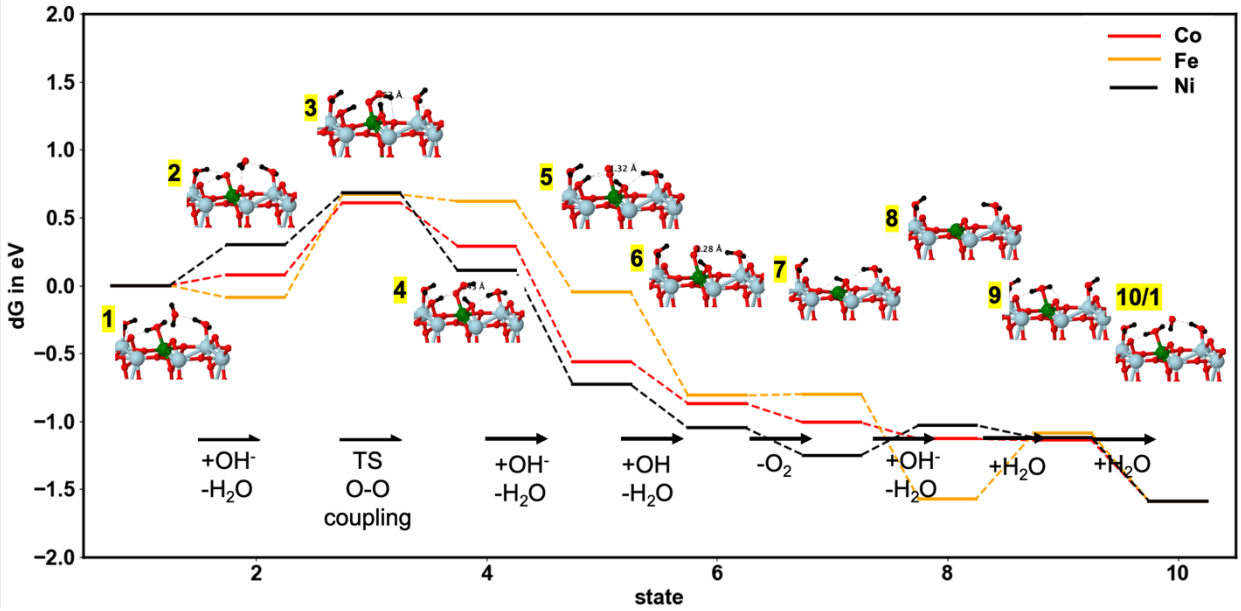

Supplementary Figure 28. Free energy landscape from GCQM calculations for Fe-, Co- and Ni-TiO_2 for the 10 states involved in OER at pH=14 and applied potentials of 1.63 V_{RHE}. The green, blue, red and black spheres in the atomic models represent Co (or Fe, Ni), Ti, O and H atoms, respectively.

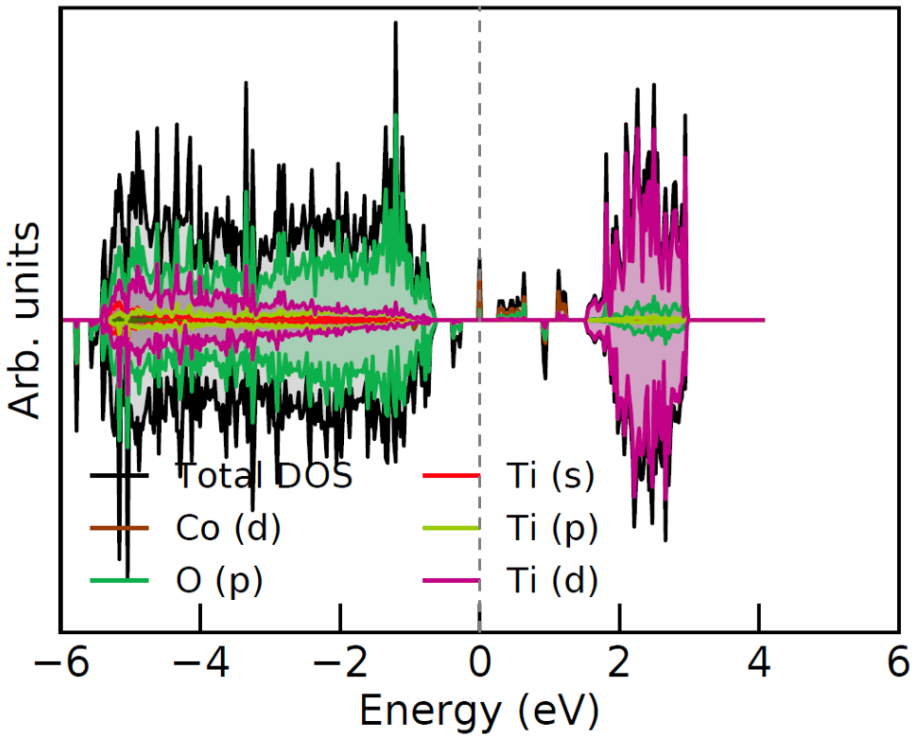

Supplementary Figure 29. DOS for group 1 catalytic surface with 12.5 % Co in the topmost layer (model is shown in Supplementary Fig. 24a).

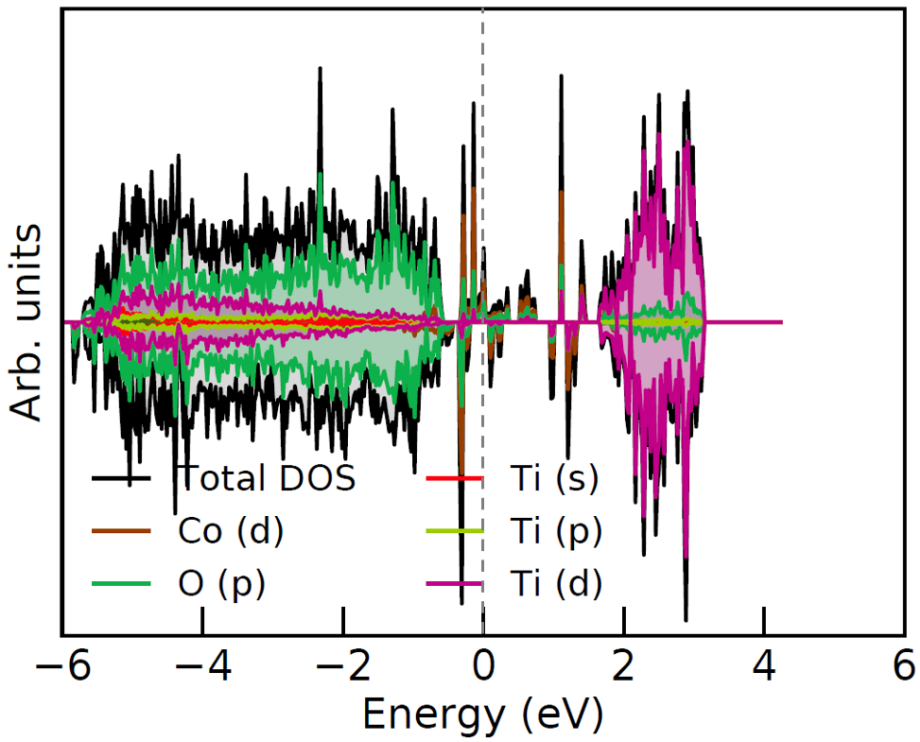

Supplementary Figure 30. DOS for group 2 catalytic surface with 12.5 % Co connecting in a line. (model is shown in Supplementary Fig. 24c).

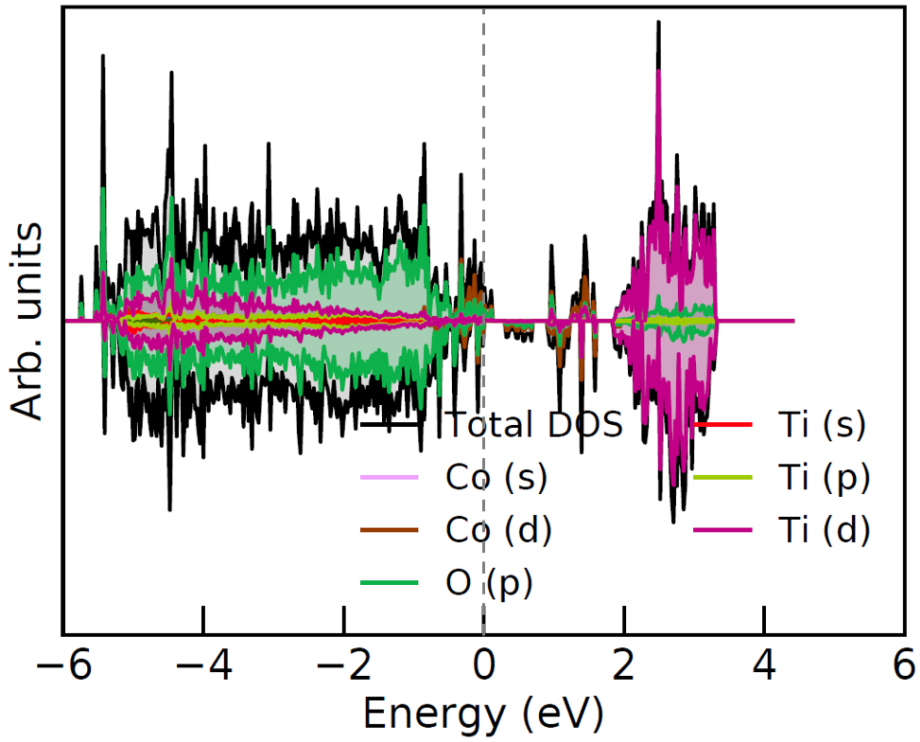

Supplementary Figure 31. DOS for group 3 catalytic surface with 12.5 % Co not in a line (model is shown in Supplementary Fig. 24d).

Supplementary References

1. Zhang, Z. et al. Generalized synthetic strategy for transition-metal-doped brookite-phase TiO_2 nanorods. *J. Am. Chem. Soc.* **141,** 16548-16552 (2019).
2. Wu, L. et al. Stable cobalt nanoparticles and their monolayer array as an efficient electrocatalyst for oxygen evolution reaction. *J. Am. Chem. Soc.* **137**, 7071-7074 (2015).
3. Sundararaman, R. & Goddard III, W. A. The charge-asymmetric nonlocally determined local-electric (CANDLE) solvation model. *J. Chem. Phys.* **142**, 064107 (2015).
4. Huang, Y., Nielsen, R. J. & Goddard III, W. A. Reaction mechanism for the hydrogen evolution reaction on the basal plane sulfur vacancy site of MoS_2 using grand canonical potential kinetics. *J. Am. Chem. Soc.* **140**, 16773–16782 (2018).
5. Xie, Y., Zhou, L., Huang, C., Huang, H., Lu, J. Fabrication of nickel oxide-embedded titania nanotube array for redox capacitance application. *Electrochim. Acta* **53**, 3643-3649 (2008).
6. Kim, J., Chen, X.; Shih, P.-C. & Yang, H. Porous perovskite-type lanthanum cobaltite as electrocatalysts toward oxygen evolution reaction. *ACS Sustain. Chem. Eng.* **5**, 10910-10917 (2017).
7. Zou, X., Goswami, A.& Asefa, T. Efficient noble metal-free (electro)catalysis of water and alcohol oxidations by zinc-cobalt layered double hydroxide. *J. Am. Chem. Soc.* **135**, 17242-17245 (2013).
8. Marsh, D. A. et al. Water oxidation using a cobalt monolayer prepared by underpotential deposition. *Langmuir* **29**, 14728-14732 (2013).
9. Qiao, C. et al. One-step synthesis of zinc-cobalt layered double hydroxide (Zn-Co-LDH) nanosheets for high-efficiency oxygen evolution reaction. *J. Mater. Chem. A* **3**, 6878-6883 (2015).
10. Han, Y., Zhai, J., Zhang, L. & Dong, S. Direct carbonization of cobalt-doped NH_2-MIL-53(Fe) for electrocatalysis of oxygen evolution reaction. *Nanoscale* **8**, 1033-1039 (2016).
11. Mehmood, R., Tariq, N., Zaheer, M., Bibi, F. & Iqbal, Z. One-pot synthesis of graphene-cobalt hydroxide composite nanosheets (Co/G NSs) for electrocatalytic water oxidation. *Sci. Rep.* **8**, 13772 (2018).
12. Tarnev, T. et al. Scanning electrochemical cell microscopy investigation of single ZIF-derived nanocomposite particles as electrocatalysts for oxygen evolution in alkaline media. *Angew. Chem. Int. Ed.* **58**, 14265-14269 (2019).
13. Aiyappa, H. B. et al. Oxygen evolution electrocatalysis of a single MOF-derived composite nanoparticle on the tip of a nanoelectrode. *Angew. Chem. Int. Ed.* **58**, 8927-8931 (2019).
14. He, J. et al. Structure-property relationship of graphene coupled metal (Ni, Co, Fe) (oxy)hydroxides for efficient electrochemical evolution of oxygen. *J. Catal.* **377**, 619-628 (2019).
15. Zhang, Y. X. et al. A novel electrocatalyst for oxygen evolution reaction based on rational anchoring of cobalt carbonate hydroxide hydrate on multiwall carbon nanotubes. *J. Power Sources* **278**, 464-472 (2015).
16. Xiao, Q. et al. A high-performance electrocatalyst for oxygen evolution reactions based on electrochemical post-treatment of ultrathin carbon layer coated cobalt nanoparticles. *Chem. Comm.* **50**, 13019-13022 (2014).

17. Liu, P. F., Yang, S., Zheng, L. R., Zhang, B. & Yang, H. G. Electrochemical etching of α-cobalt hydroxide for improvement of oxygen evolution reaction. *J. Mater. Chem. A* **4**, 9578-9584 (2016).
18. Song, F. & Hu, X. Ultrathin cobalt-manganese layered double hydroxide is an efficient oxygen evolution catalyst. *J. Am. Chem. Soc.* **136**, 16481-16484 (2014).
19. Bähr, A., Moon, G.-h. & Tüysüz, H. Nitrogen-doped mesostructured carbon-supported metallic cobalt nanoparticles for oxygen evolution reaction. *ACS Appl. Energy Mater.* **2**, 6672-6680 (2019).
20. Qiu, C. et al. 2-Methylimidazole directed ambient synthesis of zinc-cobalt LDH nanosheets for efficient oxygen evolution reaction. *J. Colloid Interface Sci.* **565**, 351-359 (2020).
21. Xun, S. et al. MOF-derived cobalt oxides nanoparticles anchored on $CoMoO_4$ as a highly active electrocatalyst for oxygen evolution reaction. *J. Alloys Compd.* **806,** 1097-1104 (2019).
22. Li, Z. et al. Co_3O_4 nanoparticles with ultrasmall size and abundant oxygen vacancies for boosting oxygen involved reactions. *Adv. Funct. Mater.* **29**, 1903444 (2019).
23. Zha, Q., Xu, W., Li, X. & Ni, Y. Chlorine-doped α-$Co(OH)_2$ hollow nano-dodecahedrons prepared by a ZIF-67 self-sacrificing template route and enhanced OER catalytic activity. *Dalton Trans.* **48**, 12127-12136 (2019).
24. Surendranath, Y., Kanan, M. W. & Nocera, D. G. Mechanistic studies of the oxygen evolution reaction by a cobalt-phosphate catalyst at neutral pH. *J. Am. Chem. Soc.* **132**, 16501-16509 (2010).
25. Lyu, F. et al. Self-templated fabrication of CoO–MoO_2 nanocages for enhanced oxygen evolution. *Adv. Funct. Mater.* **27**, 1702324 (2017).
26. Cao, Y.et al. Ionic liquid-assisted one-step preparation of ultrafine amorphous metallic hydroxide nanoparticles for the highly efficient oxygen evolution reaction. *J. Mater. Chem. A* https://doi.org/10.1039/D0TA00434K (2020).
27. Gao, Z. et al. Flexible and robust bimetallic covalent organic framework for reversible switching of electrocatalytic oxygen evolution activity. *J. Mater. Chem. A* **8,** 5908-5912 (2020).
28. Yang, M. et al. Synchronously integration of Co, Fe dual-metal doping in Ru@C and CDs for boosted water splitting performances in alkaline media. *Appl. Catal., B* **267**, 118657 (2020).
29. Li, C. et al. Hierarchically structured two-dimensional bimetallic CoNi-hexaaminobenzene coordination polymers derived from $Co(OH)_2$ for enhanced oxygen evolution catalysis. *Small* **16**, 1907043 (2020).
30. Huang, J. et al. Controlled synthesis of hollow bimetallic prussian blue analog for conversion into efficient oxygen evolution electrocatalyst. *ACS Sustain. Chem. Eng.*. **8**, 1319-1328 (2020).
31. Xu, S. et al. Pressure-driven catalyst synthesis of Co-doped Fe_3C@carbon nano-onions for efficient oxygen evolution reaction. *Appl. Catal., B* **268**, 118385 (2020).
32. Zhang, R., Cheng, S., Li, N. & Ke, W. N, S-codoped graphene loaded Ni-Co bimetal sulfides for enhanced oxygen evolution activity. *Appl. Surf. Sci.* **503**, 144146 (2020).
33. Mahala, C., Sharma, R., Sharma, M. D. & Pande, S. Development of copper cobalt sulfide with Cu : Co Ratio variation on carbon cloth as an efficient electrode material for the oxygen evolution reaction. *ChemElectroChem* **6**, 5301-5312 (2019).

34. Song, Q. et al. Enhanced electrocatalytic performance through body enrichment of Co-based bimetallic nanoparticles in situ embedded porous N-doped carbon spheres. *Small* **15**, 1903395 (2019).
35. Qin, C. et al. Amorphous NiMS (M: Co, Fe or Mn) holey nanosheets derived from crystal phase transition for enhanced oxygen evolution in water splitting. *Electrochim. Acta* **323**, 134756 (2019).
36. Wang, X. et al. Synthesis and identifying the active site of Cu_2Se@CoSe nano-composite for enhanced electrocatalytic oxygen evolution. *Electrochim. Acta* **320**, 134589 (2019).
37. Yu, X. et al. Microstructural engineering of heterogeneous P−S−Co interface for oxygen and hydrogen evolution. *ChemElectroChem* **6**, 3708-3713 (2019).
38. Zhang, Y. et al. Rock salt type $NiCo_2O_3$ supported on ordered mesoporous carbon as a highly efficient electrocatalyst for oxygen evolution reaction. *Appl. Catal., B* **256**, 117852 (2019).
39. Li, R. et al. Anion–cation double doped Co_3O_4 microtube architecture to promote high-valence Co species formation for enhanced oxygen evolution reaction. *ACS Sustain. Chem. Eng.* **7**, 11901-11910 (2019).
40. Liu, Y. et al. Small sized Fe–Co sulfide nanoclusters anchored on carbon for oxygen evolution. *J. Mater. Chem. A* **7**, 15851-15861 (2019).
41. Amorim, I. et al. Bi-metallic cobalt-nickel phosphide nanowires for electrocatalysis of the oxygen and hydrogen evolution reactions. *Catal. Today* https://doi.org/10.1016/j.cattod.2019.05.037 (2019).
42. Roy, C. et al. Impact of nanoparticle size and lattice oxygen on water oxidation on $NiFeO_xH_y$. *Nat. Catal.* **1**, 820-829 (2018).
43. Yeo, B. S.& Bell, A. T. Enhanced activity of gold-supported cobalt oxide for the electrochemical evolution of oxygen. *J. Am. Chem. Soc.* **133**, 5587-5593 (2011).
44. Burke, M. S., Kast, M. G., Trotochaud, L., Smith, A. M. & Boettcher, S. W. Cobalt-iron (oxy)hydroxide oxygen evolution electrocatalysts: the role of structure and composition on activity, stability, and mechanism. *J. Am. Chem. Soc.* **137**, 3638-3648 (2015).
45. Li, P. et al. Probing enhanced site activity of Co–Fe bimetallic subnanoclusters derived from dual cross-linked hydrogels for oxygen electrocatalysis. *ACS Energy Lett.* **4**, 1793-1802 (2019).
46. Liu, Y. et al. Polyoxoniobate ion-assisted electrodeposition of cobalt and nickel water oxidation catalysts. *ACS Appl. Mater. Interfaces* **7**, 16632-16644 (2015).
47. Han, J. et al. Zn doped FeCo layered double hydroxide nanoneedle arrays with partial amorphous phase for efficient oxygen evolution reaction. *ACS Sustain. Chem. Eng.* **7**, 13105-13114 (2019).
48. Mao, H. et al. Efficiently improving oxygen evolution activity using hierarchical α-$Co(OH)_2$/polypyrrole/graphene oxide nanosheets. *Appl. Surf. Sci.* **485**, 554-563 (2019).
49. Xie, L. et al. High-performance electrolytic oxygen evolution in neutral media catalyzed by a cobalt phosphate nanoarray. *Angew. Chem. Int. Ed.* **56**, 1064-1068 (2017).
50. Chou, N. H., Ross, P. N., Bell, A. T. & Tilley, T. D. Comparison of cobalt-based nanoparticles as electrocatalysts for water oxidation. *ChemSusChem* **4**, 1566-1569 (2011).
51. Lin, Q. et al. Hierarchical amorphous carbon-coated Co/Co_9S_8 nanoparticles on MoS_2 toward synergetic electrocatalytic water splitting. *Ind. Eng. Chem. Res.* **58**, 23093-23098 (2019).

52. Zhang, G., Wang, B, Li, L. & Yang, S. Phosphorus and yttrium codoped Co(OH)F nanoarray as highly efficient and bifunctional electrocatalysts for overall water splitting. *Small* **15**, 1904105 (2019).
53. Kim, H. J. et al. Enhanced activity and stability of TiO_2-coated cobalt/carbon catalysts for electrochemical water oxidation. *ACS Catal.* **5**, 3463-3469 (2015).
54. Burke, M. S., Kast, M. G., Trotochaud, L., Smith, A. M. & Boettcher, S. W. Cobalt–iron (oxy)hydroxide oxygen evolution electrocatalysts: the role of structure and composition on activity, stability, and mechanism. *J. Am. Chem. Soc.***137**, 3638-3648 (2015).
55. Yang, M. et al. Superior oxygen evolution reaction performance of Co_3O_4/$NiCo_2O_4$/Ni foam composite with hierarchical structure. *ACS Sustain. Chem. Eng.* **7**, 12214-12221 (2019).
56. Tian, Y. et al. Superaerophobic quaternary Ni–Co–S–P nanoparticles for efficient overall water-splitting. *ACS Sustain. Chem. Eng.* **7**, 14639-14646 (2019).
57. Zhang, C., Tang, B., Gu, X. & Feng, L. Surface chemical state evaluation of CoSe2 catalysts for the oxygen evolution reaction. *Chem. Commun.* **55**, 10928-10931 (2019).
58. Li, Q., Tang, S., Tang, Z., Zhang, Q. & Yang, W. Microwave-assisted synthesis of $FeCoS_2$/XC-72 for oxygen evolution reaction. *Solid State Sci.* **96,** 105968 (2019).
59. Yang, W. et al. Defect engineering of cobalt microspheres by S doping and electrochemical oxidation as efficient bifunctional and durable electrocatalysts for water splitting at high current densities. *J. Power Sources* **436**, 226887 (2019).
60. Liang, D. et al. Interfacial charge polarization in $Co_2P_2O_7$@N, P co-doped carbon nanocages as Mott-Schottky electrocatalysts for accelerating oxygen evolution reaction. *Appl. Catal., B* **268**, 118417 (2020).
61. Su, H. et al., Hetero-N-coordinated Co single sites with high turnover frequency for efficient electrocatalytic oxygen evolution in an acidic medium. *ACS Energy Lett.* **4**, 1816-1822 (2019).
62. Ma, X. et al. The surface engineering of cobalt carbide spheres through N, B co-doping achieved by room-temperature in situ anchoring effects for active and durable multifunctional electrocatalysts. *J. Mater. Chem. A* **7**, 14904-14915 (2019).
63. Liu, P. et al. Cu and Co nanoparticle-Co-decorated N-doped graphene nanosheets: a high efficiency bifunctional electrocatalyst for rechargeable Zn–air batteries. *J. Mater. Chem. A* **7**, 12851-12858 (2019).
64. He, Y. et al. Charge redistribution of Co on cobalt (II) oxide surface for enhanced oxygen evolution electrocatalysis. *Nano Energy* **61**, 267-274 (2019).
65. Zhang, Q.; Liu, N.; Guan, J., Accelerative oxygen evolution by Cu-doping into Fe-Co oxides. *Sustainable Energy & Fuels***, 4**, 143-148 (2020).